PERGAMON

Acta mater. 48 (2000) 1259–1271

Acta MATERIALIA

www.elsevier.com/locate/actamat

DEFORMATION AND FAILURE MECHANISMS OF BRAIDED COMPOSITE TUBES IN COMPRESSION AND TORSION

A.-M. HARTE and N. A. FLECK†

Cambridge Centre for Micromechanics, Cambridge University Engineering Department, Trumpington Street, Cambridge CB2 1PZ, UK

(Received 21 May 1999; received in revised form 11 November 1999; accepted 11 November 1999)

Abstract—The deformation and fracture behaviour of glass fibre–epoxy braided circular tubes is examined experimentally and theoretically for the loading cases of compression, torsion, and combined tension–torsion and compression–torsion. Failure maps are produced for compression and for torsion to summarise the effect of braid microstructure upon failure mode and upon the mechanical properties of the braid, including yield strength, modulus, strain to failure and energy absorption. In compression, two competing mechanisms are observed: diamond shaped buckling of the tube and fibre microbuckling. In torsion and in combined compression–torsion, the tubes fail by fibre microbuckling. The initiation and propagation stresses for diamond shaped buckling, and the critical stress for fibre microbuckling are successfully predicted using simple micromechanical models. Drawing upon the available experimental data, yield surfaces are constructed for in-plane loading of the braid, and a comprehensive mechanism map is constructed to illustrate the dependence of failure mode upon braid geometry and loading direction.

Keywords: Braided composite; Fracture; Structural behaviour

1. INTRODUCTION

Traditional fibre composites are fabricated by laying up pre-impregnated plies of aligned fibres. In this way the strength and stiffness of the composite can be tailored in given directions. Textile composites are manufactured by fabrication methods derived from the textile industry: weaving, knitting, stitching and braiding. This paper focuses on braided textile composites. Bundles of fibres, termed tows, are interlaced in the same way that the ribbons in the maypole dance are interlaced, resulting in a woven tubular structure. Textile composites offer many advantages over traditional laminated composites. Laminated composites have low toughness against in-plane splitting and suffer from delamination between plies. In textile composites, the inter-lacing of the tows in the through-thickness direction increases the splitting toughness and largely eliminates the delamination problem. The manufacture of laminated composites is labour intensive and as a result the cost is high, but for many applications braided composites can be fabricated directly into net shape, decreasing the manufacturing time and cost. Textile composite structures are lightweight and can provide high crashworthiness when used as part of an energy dissipating device, such as the sub-floor assembly of helicopter cabins [1]. Braided composite tubes offer better energy-management characteristics than laminated composites, because the intertwining fibre architecture prevents gross delamination, as discussed by Hamada *et al.* [2].

Much effort has been spent in modelling the elastic bulk properties of woven and braided composites based on laminate plate theory [3], but comparatively little work has been done in understanding the micro-mechanics of deformation. Here, we examine the deformation and fracture responses of a regular glass fibre braid under compression and torsion. The failure mode and associated failure strength of braided circular tubes are dependent on the tow geometry, matrix material, tube geometry, and on the loading direction. To assess these dependencies, circular braided tubes with a range of initial helix angles were tested in compression, torsion and in combined loading. (The helix angle is defined as the angle between the tows in a braid and the

† To whom all correspondence should be addressed. Tel.: +44-1223-332650; fax: +44-1223-332662.

E-mail address: naf1@eng.cam.ac.uk (N.A. Fleck).

1359-6454/00/$20.00
PII: S1359-6454(99)00427-9

longitudinal axis of the cylinder, as shown in Fig. 1.) The stress–strain response of glass fibre–epoxy braided tubes is reported for a range of loadings: compression, torsion and combined loading. For each loading direction, charts are constructed from experimental observations to show the dependence of braid properties and operative failure mechanism upon helix angle. Tension–torsion and compression–torsion experiments were also performed, and a yield surface is constructed in stress-space for each initial helix angle tested. A failure mechanism map, which takes as axes the helix angle and the direction of loading, is constructed from the experimental data from this work and also from tension tests presented in a companion paper [4].

After the experimental results have been presented, simple micromechanical models are described for failure of the circular braided tubes under compressive and shear loadings. The competing failure modes in compression are Euler buckling, diamond shaped buckling of the tube, and fibre microbuckling. The microbuckling phenomenon involves the co-operative buckling of fibres within a narrow band [5]. The critical stress required to initiate microbuckling under compressive or shear loading is determined, and the sensitivity of the microbuckling stress to the fibre waviness angle of the cross-over points of tows is emphasised. A failure map is constructed to show the competition between Euler buckling, diamond shaped buckling and microbuckling with regard to shape of the tube and a structural load index.

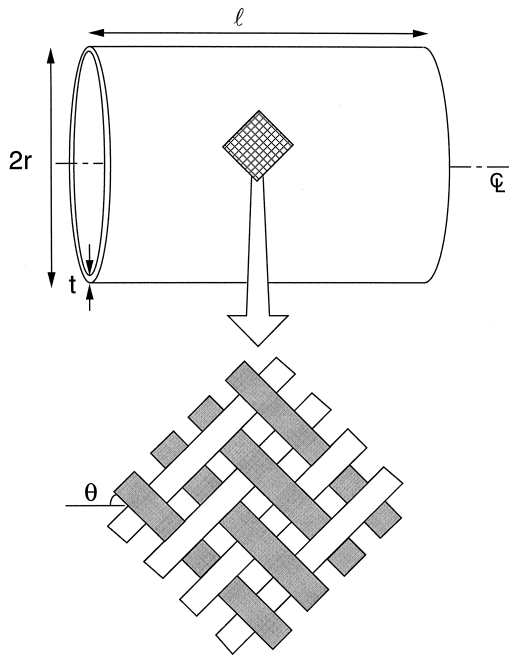

Fig. 1. Overall geometry and fibre architecture of a braided tube of radius r, wall thickness t, length ℓ, and helix angle θ.

2. MATERIALS

Braids with a "two-over-two-under" architecture, known in the literature as regular braids were manufactured in-house from 1.6 k glass fibre tow and cast in an epoxy matrix (see Fig. 1). Specimens of circular cylindrical geometry were braided from a single layer of 32 tows in the $+\theta$ direction and 32 tows in the $-\theta$ direction. The helix angle θ of the braid was controlled by expanding the braid over cylindrical mandrels of various diameters before casting with epoxy. The minimum achievable helix angle was $\theta = 21^\circ$ and the maximum was approximately 55°. The glass fibre volume fraction of the regular braids was held constant at 40%.

2.1. Specification of fibre and matrix

E-glass fibre tows were used as the braiding material. Each tow was a bundle of 1600 untwisted glass fibres, and each fibre was of diameter 18.9 μm. A uniaxial tension test was performed on a single tow: it was linear elastic to fracture with a measured modulus of 63 GPa and a tensile strength of 1.9 GPa.

The matrix was a two part casting epoxy comprised of Ciba-Geigy Araldite MY 753 with HY 956 hardener, mixed 100 parts to 20 parts by volume. The epoxy was brushed onto the dry braid cylinders and allowed to wick into the tows. The cylinders were then cured in an air oven at 100°C for 20 min. Microscopic examination revealed that the level of porosity within the matrix was minimal (less than 1%).

In order to determine the tensile and compressive stress–strain response of the cured epoxy, uniaxial tensile tests were performed on dog-bone specimens of cured epoxy with rectangular section 5 mm × 3 mm and gauge-length 25 mm, at a strain rate of 0.003/s. Compression tests were done on cubes with side length 19.0 mm, at a strain rate of 0.003/s. The results are shown in Fig. 2. In tension, the epoxy failed in a brittle manner, presumably from a pre-existing defect, at a tensile stress of 43 MPa. In

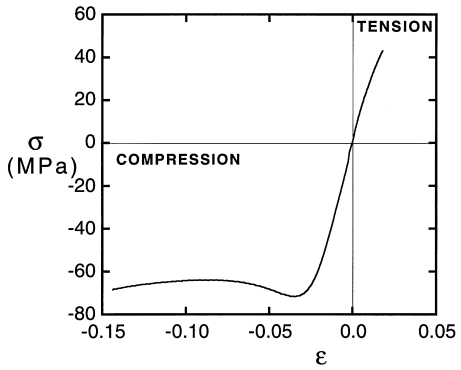

Fig. 2. Uniaxial nominal stress vs nominal strain behaviour of the epoxy, at a nominal strain rate of 0.003/s.

Table 1. Dimensions of specimens for each type of test, along with the load and shape factors for the shape efficiency map given in Fig. 12

Helix angle θ_o	Diameter $2r$ (mm)	Wall thickness t (mm)	Compressive specimens	Torsion and compression/torsion specimens	Load factor $P/k\ell^2$	Shape factor Φ
			Gauge length ℓ (mm)	Gauge length ℓ (mm)		
23°	25.37	1.20	25	28	0.77	10.5
30°	31.75	1.15	35	N/A	0.35	13.2
40°	42.20	0.98	42	47	0.20	17.5
55°	53.0	0.93	53	58	0.22	22

compression, it exhibits a relatively ductile response due to shear yielding; the upper yield strength in compression is 72 MPa and the Young's modulus E equal to 2.8 MPa.

3. EXPERIMENTS

The load vs displacement response was measured for circular braided tubes over a wide range of helix angles and for the loading states of uniaxial compression, torsion and for combined compression–torsion and tension–torsion. For uniaxial compression and torsion, failure maps were produced from the experimental data to display the effect of helix angle on modulus, yield strength, strain to failure and energy absorption.

3.1. Uniaxial compression response

The effect of initial helix angle on the compressive response of the braided glass–epoxy tubes is reported in this Section. Compressive tests were

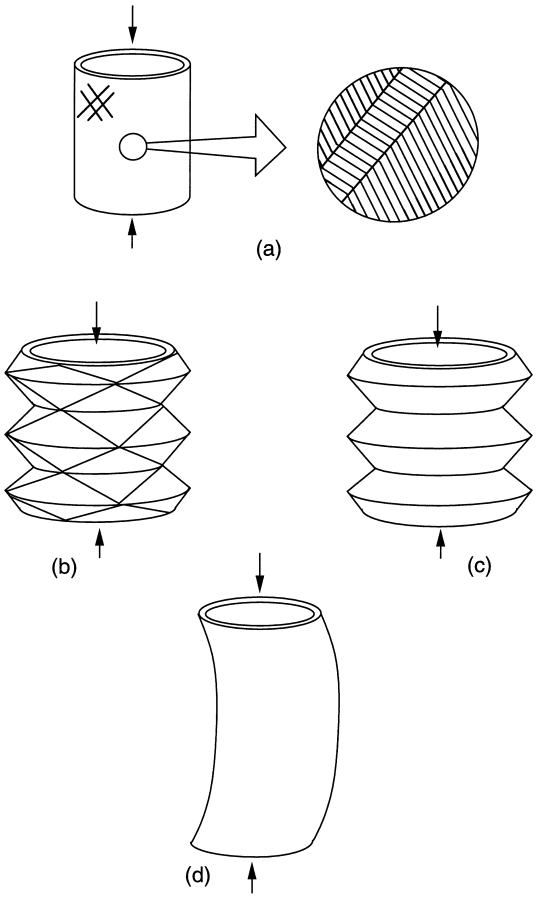

Fig. 3. The four possible modes of buckling for braided circular tubes in axial compression. (a) Fibre microbuckling, (b) diamond shaped buckling, (c) concertina buckling and (d) Euler macrobuckling.

conducted between parallel platens using a PTFE lubricating spray.

3.1.1. Experimental procedure. Regular braids, with initial helix angles θ_o in the range 23°–55° and with dimensions given in Table 1, were compressed to failure between parallel, lubricated platens using a screw-driven test machine and a cross-head speed of 0.033 mm/s. The specimens were machined so that their lengths were approximately equal to their diameters, in order to prevent Euler buckling. The cross-head displacement of the test machine was used to measure the large axial nominal strains associated with the post-buckling collapse; the nominal compressive stress is defined by the measured load divided by the original cross-sectional area of the tube wall.

3.1.2. Experimental results. Figure 3 shows four possible failure modes of braided tubes in compression: (a) microbuckling, (b) diamond shaped buckling, (c) concertina buckling and (d) Euler buckling. Microbuckling is a localised material instability involving the rotation of fibres within a narrow band of width about 20 fibre diameters, as shown in Fig. 3(a). The stress level for activation of this failure mode depends upon the in-plane shear strength of the composite along the local fibre direc-

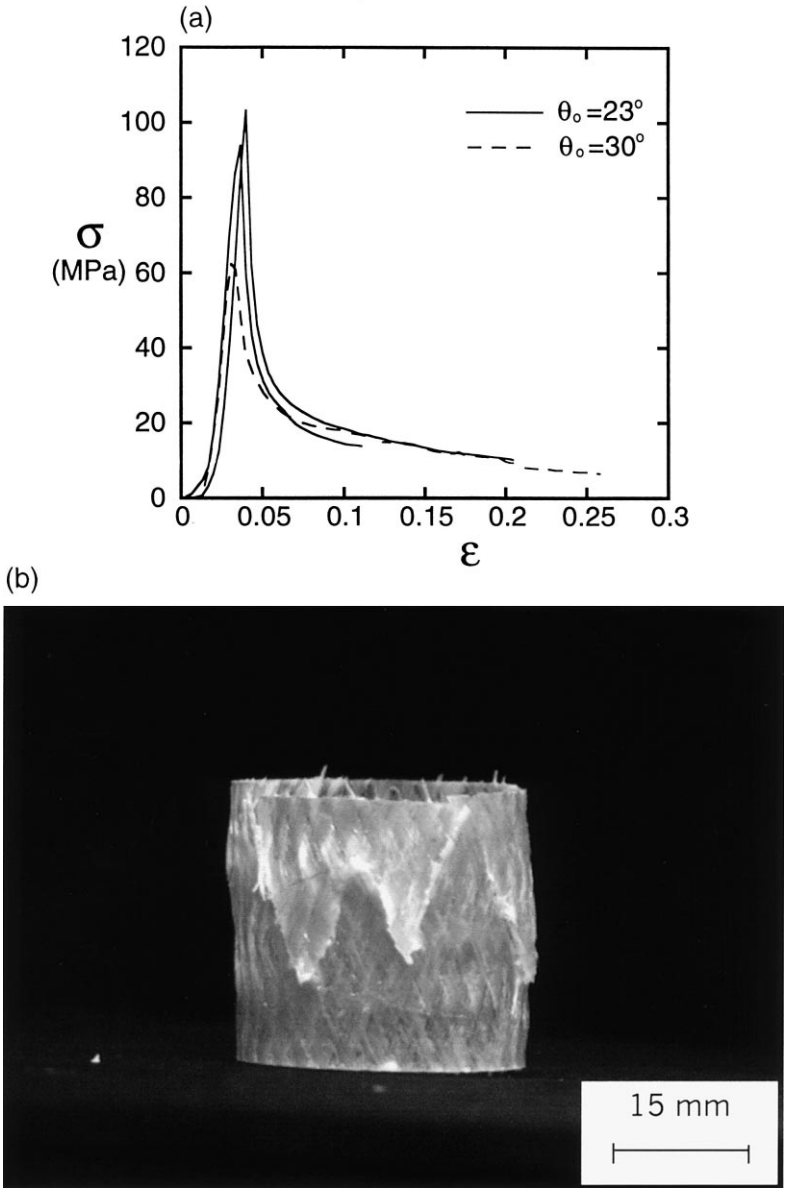

Fig. 4. (a) Nominal stress–nominal strain behaviour for braids of initial helix angle $\theta_o = 23°$ and 30° failing by microbuckling in compression. (b) The sawtooth fracture path of a compressive specimen which has failed by microbuckling.

tion, and the magnitude of any imperfection such as fibre waviness, as reviewed by Fleck [5], for example. Diamond shaped buckling and concertina buckling are two competing shell-buckling modes [see Fig. 3(b),(c)]; the axial collapse load and the buckle wavelength depend upon both the diameter of the tube and the wall thickness. The dominant mode depends upon the aspect ratio of wall thickness to diameter, and upon the ratio of circumferential to axial stiffness of the tube. Euler macrobuckling [Fig. 3(d)] involves buckling of the whole cross-section of the tube; unlike the other modes, the collapse load is sensitive to the length of the tube. In the current investigation on braided composite tubes, microbuckling was observed for a braid angle $\theta_o < 35^\circ$, whereas diamond shaped buckling was observed for $\theta_o > 35^\circ$.

1. *Microbuckling: regular braids with* $\theta_o < 35^\circ$. The braids of angle $\theta_o = 23^\circ$ and 30° failed by microbuckling, and the measured nominal stress-nominal strain responses are given in Fig. 4(a). They consist of a single peak with a long tail. The residual compressive strength at the end of the test is associated with frictional sliding of the failure surfaces past each other. Out-of-plane microbuckles formed within individual tows near the cross-over point with another tow, creating a sawtooth pattern around the specimen, as shown in Fig. 4(b). The scatter is small as illustrated by the repeat test for $\theta_o = 23^\circ$.

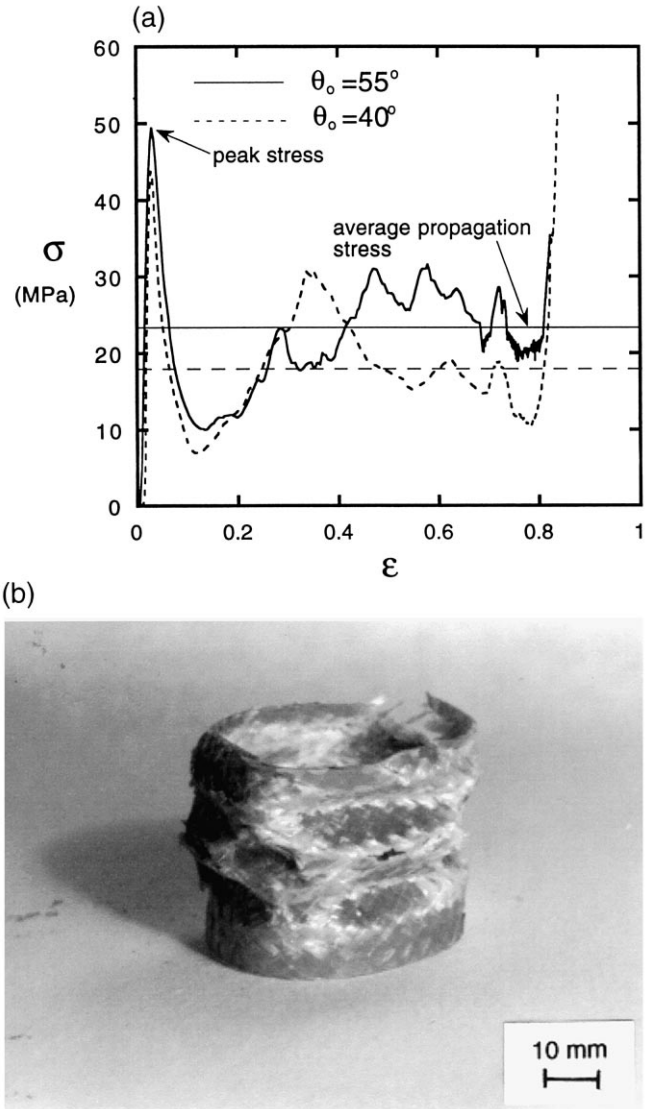

Fig. 5. (a) Compressive nominal stress vs nominal strain curves for braided tubes with braid angles $\theta_o = 40^\circ$ and 55° which have failed by diamond shaped buckling. (b) Photograph of a $\theta_o = 40^\circ$ braid which has failed by diamond shaped buckling.

2. *Diamond shaped buckling: regular braids with* $\theta_o > 35^\circ$. The braids of initial helix angle $\theta_o = 40^\circ$ and 55° collapsed by a diamond shaped buckling mode; the associated nominal stress–nominal strain curves are shown in Fig. 5(a). Collapse by diamond shaped buckling involves localised buckling along diagonal lines on the surface of the cylinders, as shown in a photo of a compressed braid in Fig. 5(b). The nominal stress vs nominal strain curve displays an initial peak corresponding to the initiation of buckling. The folding pattern propagates along the length of the specimens until the entire cylinder has collapsed. The subsequent load maxima after the initial peak in the stress–strain curve correspond to the triggering of consecutive bands of folding in the cylinder. After each fold has formed and has locked-up, the nominal stress–nominal strain curve turns upwards until the load is sufficient for the next fold to form, causing an oscillating load response.

3.1.3. Failure charts. The main details of the collapse response in uniaxial compression tests are summarised as a failure chart in Fig. 6. The figure takes as abscissa the initial helix angle, and as ordinate the axial modulus E, the failure stress σ_f, nominal strain to failure ϵ_f, and specific energy absorption W. The failure stress is the peak strength, and W is the absorbed energy per unit initial volume of braid-wall material. Error bars have been added to display the degree of material scatter.

Consider the failure chart for simple compression given in Fig. 6. The two competing modes of failure are microbuckling and diamond shaped buckling. There is a trade-off between strength and stiffness on the one hand, and ductility and energy absorption on the other. The braids with small helix angles ($\theta_o = 23^\circ$, 30°) fail by microbuckling and have the highest strengths, but lowest strains to failure ϵ_f. The switch to diamond shaped buckling is associated with a large decrease in collapse stress, but a dramatic increase in the strain to failure. Since diamond shaped buckling causes more diffuse damage to a tube than microbuckling, it is not surprising that it absorbs much more energy.

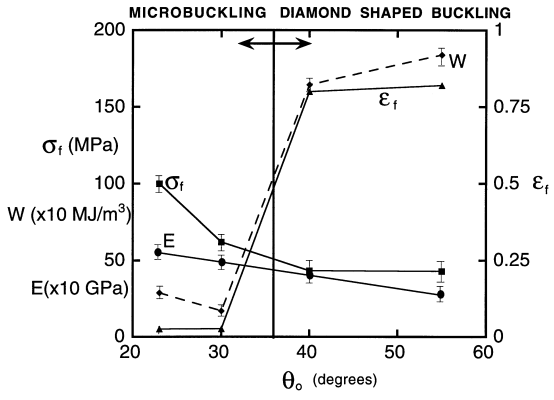

Fig. 6. Failure chart of braided tubes in compression. Microbuckling and diamond shaped buckling are the two competing modes of failure.

3.2. Torsion

3.2.1. Experimental procedure. Three braids with helix angles $\theta_o = 23^\circ$, 40° and 55° were loaded in torsion to failure in a servo-hydraulic tension–torsion test machine. The ends of the samples were glued to cylindrical grips using epoxy adhesive in combination with jubilee clips. The axial cross-head was held at zero load in load-control to ensure a state of pure torsion, and the cross-head was rotated in rotation-control at a rate of about 0.005 rad/s. Macrobuckling of the specimen was prevented by choosing its length to be comparable with its diameter, as summarised in Table 1.

In order to measure the average strain response of the specimen, strain gauge rosettes of length

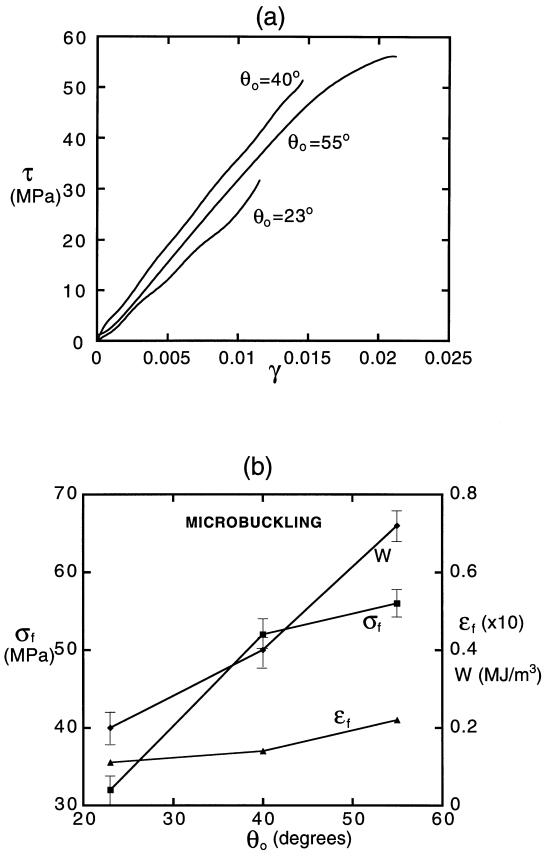

Fig. 7. (a) Shear stress–strain curves for braids under torsional loading. (b) Failure chart of braided cylinders under torsional loading. Microbuckling is the only failure mode observed.

10 mm and single strain gauges of gauge length 3 mm were used. The strain gauge rosettes were capable of measuring strains of up to 20%, and were used to measure the average strain in the braid in the axial and hoop directions. The large gauge length is necessary so that the local inhomogeneous straining of the matrix and individual tows do not overwhelm the average value. The smaller, single strain gauges were bonded on top of individual tows in order to measure the strain in the fibre direction.

3.2.2. Experimental results. The shear stress–shear strain curves for braids of three different angles θ_o are shown in Fig. 7(a). Here, shear stress is defined with respect to the initial wall thickness and tube radius. The shear strain is the nominal engineering value, deduced from the strain gauge measurements. It can be seen from the shear stress–strain curves that the response is almost linear-elastic to failure. The macroscopic failure plane follows that of a helical tow, and failure is by microbuckling at tow crossover points.

The failure chart for torsional loading is shown in Fig. 7(b). We note that the failure strength σ_f, specific energy W, and failure strain ϵ_f increase monotonically with increasing initial helix angle θ_o. A theoretical model of fibre microbuckling is in line with these measurements, as detailed below.

3.3. Combined loading tests

In order to explore the dependence of failure mode on stress path, tension–torsion and compression–torsion tests were performed on braided circular tubes of helix angles $\theta_o = 23^\circ$, 40° and 55°. The experimental arrangement was identical to that described for pure torsion in the previous Section, with the dimensions of the specimens again given in Table 1. The tests were performed by holding the axial load at a pre-determined value within the uniaxial elastic limit of the specimen, and then twisting the specimen to failure in rotation control.

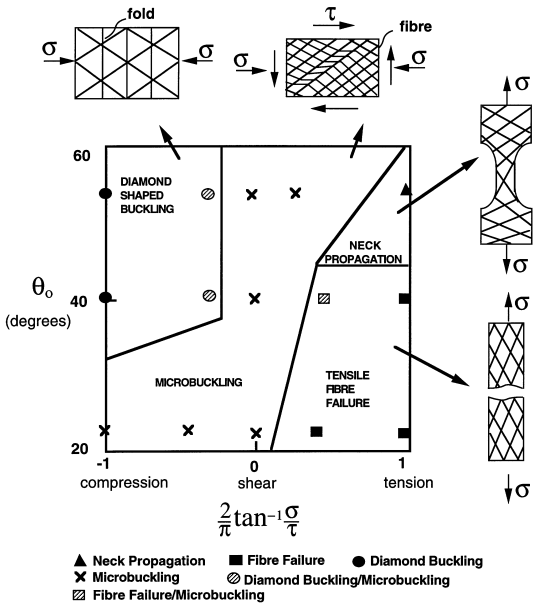

Fig. 8. Multi-axial failure mechanism map. The boundaries between failure modes depend upon both the initial helix angle θ_o and the loading path.

3.3.1. Experimental observations. For both the tension–torsion and compression–torsion tests, the stress–strain response is almost linear elastic to failure, with the failure mode strongly dependent upon helix angle. In tension–torsion, the braid of initial helix angle $\theta_o = 55^\circ$ failed by microbuckling, whereas the $\theta_o = 23^\circ$ braid underwent tensile fracture of the fibres. The $\theta_o = 40^\circ$ braid failed in a coupled mode in tension–torsion: microbuckling of one set of tows and fibre fracture of the tows of opposite inclination. For the case of combined compression–torsion, the $\theta_o = 23^\circ$ braid failed by microbuckling, whereas the $\theta_o = 40^\circ$ and 55° braids failed by a combination of microbuckling and diamond shaped buckling. The operative failure mechanism as a function of helix angle and load path is summarised in a fracture map (see Fig. 8). The figure includes the compression results described above, and tensile failure modes as determined by Harte and Fleck [4] in a companion study on braid behaviour under axial tension.

The failure strengths for tension, compression and combined loading are plotted in the stress space (σ,τ) in Fig. 9(a); here, σ is the nominal axial stress and τ is the nominal shear stress on the tube wall. The strength values in Fig. 9(a) relate to the peak value of collapse stress. The corresponding log–log plot of failure strain (ϵ_f,γ_f) is given in Fig. 9(b). For completeness, the data from previous tensile tests [4] are included. In tension, two competing modes are observed: fibre failure and neck propagation. Fibre failure occurs in tubes where the initial helix angle is less than 45°. In braids with $\theta_o > 45^\circ$, a neck forms at a point of weakness in the braid. The neck then propagates under constant load through the specimen until it has been entirely consumed, much like cold drawing in polymers. When the tensile failure mode is by fibre fracture, the observed yield strength is high, whilst the strain and energy to fracture are low. Conversely, neck propagation is associated with a low value of yield strength, a high value of energy absorption and a large failure strain (of the order of unity).

On taking Figs 8 and 9 together, the following general observations can be made. The highest tensile and compressive strengths are obtained by selecting a braid of small helix angle; these braids fail in tension by fibre fracture, and in compression by microbuckling. For maximum ductility and energy absorption, a braid of large helix angle is

optimal; such braids undergo necking in tension and diamond shaped buckling in compression. It is apparent from the fracture map (Fig. 8), that microbuckling is a dominant failure mode when the loading involves a compressive component (such as simple shear).

Harte and Fleck [4] have already developed models of tensile failure by fibre fracture and by neck propagation. In the following Section, we summarise simple engineering models of failure by diamond shaped buckling and by fibre microbuckling. The models have been used to guide the shape of the boundaries between competing failure modes in Fig. 8.

4. MODELS FOR DIAMOND SHAPED BUCKLING AND MICROBUCKLING

4.1. Compressive failure by diamond shaped buckling

Diamond shaped buckling requires an understanding of buckle initiation in the tube wall and subsequently of buckle propagation along the axis of the specimen. Both buckle initiation and buckle propagation have been widely studied problems for metallic tubes, and simple models from the literature are detailed here.

4.1.1. Initiation stress. Timoshenko and Gere [6] have used an energy method to calculate the axial stress σ_{cr} in the tube wall for elastic buckling of an isotropic circular cylinder. They find

$$\sigma_{cr} = \frac{Et}{r\sqrt{3(1-\nu^2)}} \tag{1}$$

where E is the Young's modulus, ν is the Poisson's ratio of the tube material, and r and t are the radius and wall thickness of the tube, respectively.

Experimental measurements [6] of the critical stress σ_{cr} for isotropic tubes fall well below those predicted by equation (1). The discrepancy comes

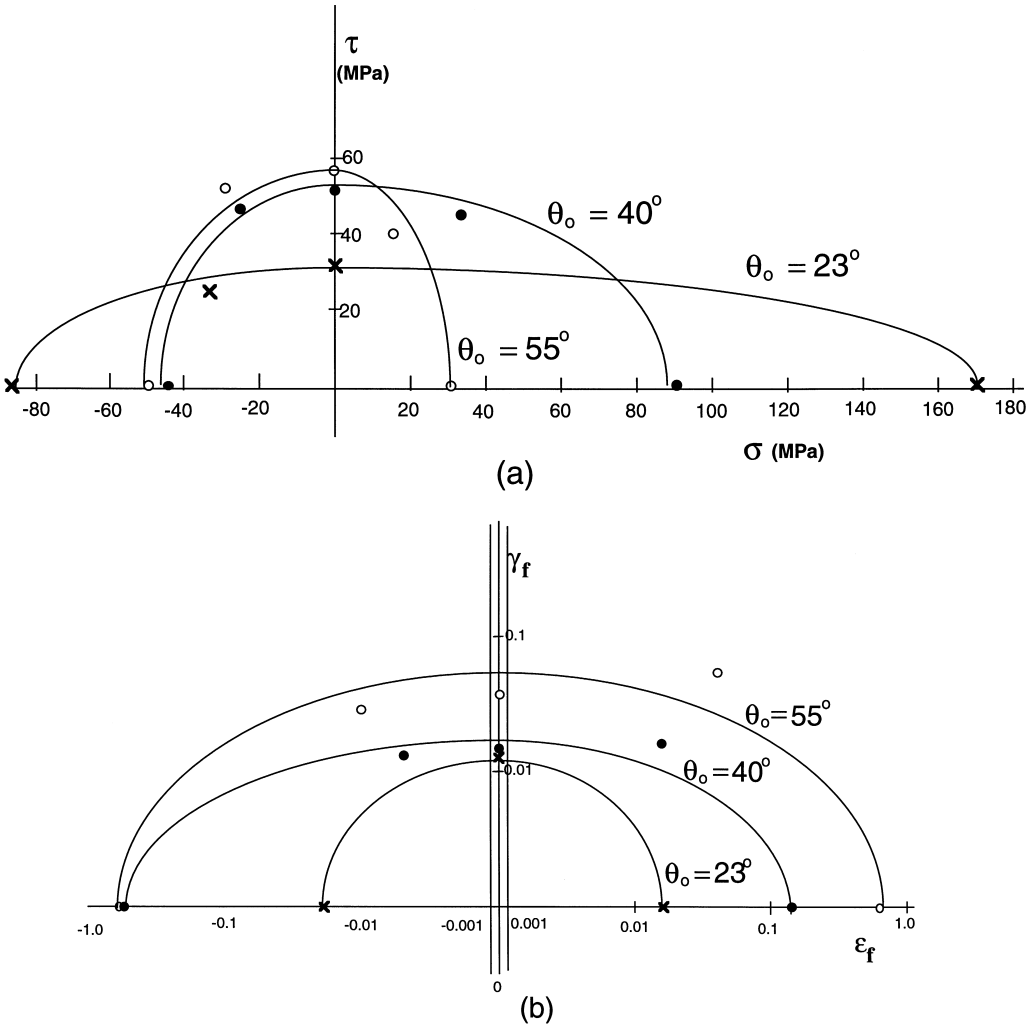

Fig. 9. Failure surfaces in (a) stress space and (b) strain state for each braid angle studied: $\theta_o = 23°$, 40°, 55°.

from two sources [7]. The first is imperfections in the tube shape, and the second is associated with boundary-layer effects at the ends of the tube. Knock-down factors have been developed from experimental data to take these factors into account. For example, Weingarten *et al.* [7] write the critical buckle stress as:

$$\sigma_{cr} = \frac{\xi E t}{r\sqrt{3(1-\nu^2)}} \tag{2}$$

where the knock-down factor, ξ, is taken as:

$$\xi = 1 - 0.901(1 - e^{-\eta}) \tag{3}$$

and

$$\eta = \frac{1}{16}\sqrt{\frac{r}{t}} \tag{4}$$

The parameters ξ and η were developed by curve-fitting experimental data for a large number of metallic tubes. Thus, the above equations provide a practical design guideline for the elastic buckling of isotropic tubes.

4.1.2. Progressive failure of tubular structures by diamond shaped buckling. The average stress for the propagation of diamond shaped buckling along a circular tube has been estimated from the work done in deforming a rigid, ideally plastic circular cylinder into a buckled shape [8–10]. Pugsley and Macaulay [8] assumed that the cylindrical tube deformed into annular rings of triangular plates; the absorbed energy was partitioned into the plastic bending at the edges of the triangular plates and the plastic stretching of the plates. They neglected the work associated with bending the curved tube wall into flat plates, and estimated the average collapse stress by equating the total plastic work to the work done by the axial compressive load. Johnson *et al.* [9] extended Pugsley and Macaulay's ideas, and introduced a more sophisticated "stationary hinge" model and also a "travelling hinge" model. In both models, the buckling mode was similar to that of Pugsley and Macaulay. Here we shall employ the Johnson *et al.* [9] stationary hinge model to predict the average collapse stress for braided composite tubes.

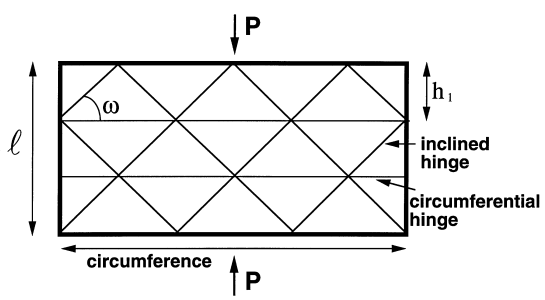

Fig. 10. A developed view of the diamond shaped buckling pattern.

A developed form of the tube is shown in Fig. 10, with the hinge pattern marked. The internal plastic work consists of bending work at the hinges between triangular plates and the work done in flattening the cylindrical tube wall into triangular plates as follows. The work done, W_1, in bending the tube into a flat plate is,

$$W_1 = 2\pi M_p \ell \tag{5}$$

where ℓ is the initial length of the tube and M_p is the plastic bending moment per unit length of the material; for a rectangular section we have $M_p = Yt^2/4$, where Y is the uniaxial yield strength of the braided tube material and t is the wall thickness. Independent uniaxial tests on the glass/epoxy braids show that they behave in an elastic–plastic ductile manner, with an axial yield strength in tension equal to that in compression; the micromechanism of plastic flow is shear yielding within the toughened epoxy matrix [11].

The second contribution to the energy absorption is that associated with bending the hinges at the edges of the triangles. There are two types of hinges: inclined and circumferential, as shown in Fig. 10. Each triangle section is bordered by two inclined hinges and one circumferential hinge. The rotation at each hinge is taken as π radians, resulting in an energy dissipation W_2 at the inclined hinges of

$$W_2 = \frac{2nmM_p\pi h_1}{\cos\,\omega} \tag{6}$$

This dissipation is for n triangles around the circumference of the tube and m rows of triangles along the length of the tube. The values of m and n depend upon the thickness to radius ratio of the tube, the presence of imperfections and the braid angle. Here, we do not attempt to predict values for n, m and the height of each triangle h_1. Instead, we shall make use of the values observed in our experiments (see Table 2). The angle ω between the inclined and circumferential hinges is given by $\pi/2n$.

The plastic work done in rotating the circumferential hinges through an angle π is

$$W_3 = (m-1)c\pi M_p \tag{7}$$

where c is the tube circumference. The average crushing force $\bar{P}$ is estimated by equating the external work on fully crushing the tube $\bar{P}\ell$ to the total energy dissipated,

$$\bar{P}\ell = W_1 + W_2 + W_3 \tag{8a}$$

giving

$$\bar{P} = 2\pi M_p\left[1 + \frac{n}{\cos\,\omega} + \frac{n}{\tan\,\omega}\,\frac{(m-1)}{m}\right] \tag{8b}$$

The above energy calculation of the average collapse load is valid both for the case where collapse is simultaneous along the length of the tube, and for the case where collapse is progressive. In reality, the collapse is progressive, beginning at one end of the tube and continuing along its length.

4.1.3. Comparison of theory with experiment for diamond shaped buckling mode. The value of the initiation stress for elastic buckling of a circular cylinder is given by equation (2). Since the knock-down parameters, ξ and η, were determined by fitting the curves to data for isotropic, homogeneous materials, it is not expected that these equations will give accurate predictions for anisotropic composite braids. A comparison is given in Table 2, where we have made use of the axial modulus in the prediction for buckling stress. The buckling stress predicted for the 40° braid is approximately twice the experimental value, but the prediction is remarkably close in the case of the 55° braid. The agreement of the theory with the measured compressive strength for the 55° braid is fortuitous. The accurate prediction of the initiation stress in structures is a notoriously difficult problem due to the strong effect of imperfections on the initiation stress.

A comparison of the predicted mean crushing stress with the measured values is included in Table 2. The simple theory appears to be adequate for modelling the experimental results, provided the buckling pattern is known.

4.2. Microbuckling

Available theoretical results for the microbuckling of laminated composites are reviewed, and the predictions from these existing models are then compared with the measured strengths of the braided composites.

4.2.1. Theory. It is generally accepted that fibre microbuckling of composites is an imperfection-sensitive, plastic buckling event involving the non-linear longitudinal shear of the composite within a narrow kink band. Argon [12] argued that the compressive strength σ_{cr} is given by

$$\sigma_{cr} = \frac{k}{\bar{\phi}} \tag{9}$$

for a composite comprising inextensional fibres and a rigid–ideally plastic matrix of shear strength k. Kinking initiates from a local region of fibre misalignment of angle $\bar{\phi}$. It is assumed that the microbuckle band is transverse to the overall fibre direction, such that the angle β between the normal to the band and the fibre direction vanishes. Now consider the case where the initial waviness angle $\bar{\phi}$ is not small, and the remote stress state consists of in-plane shear τ^{∞} in addition to a compressive stress parallel to the fibres. Then, for moderate angles, $\bar{\phi}$, Fleck and Budiansky [13] have shown that

$$\sigma_{cr} \approx \frac{k - \tau^{\infty}}{\tan\ \bar{\phi}} \tag{10}$$

Note that in the limit of vanishing τ^{∞} and small $\bar{\phi}$, the expression (10) simplifies to Argon's result (9).

4.2.2. Application of microbuckling theory to braids. An accurate prediction of the compressive strength of braided tubes is complicated by the 3D architecture of the weave. The approach adopted here is to treat the braid as a $\pm\theta$ 2D laminate comprising two angle plies, and to use laminate plate theory to estimate the stress state within each layer. Harte and Fleck [4] have already had some success in predicting effective elastic properties for the braided composite using laminate plate theory. Failure by microbuckling occurs at overall stress levels within the elastic range, and this provides some justification for the use of elastic laminate plate theory (LPT) to determine the stress state in the braid at the fracture stress.

The elastic stiffness of a single $+\theta$ or $-\theta$ ply in Cartesian axes aligned with the tow direction is deduced from the elastic properties of fibres and matrix, and is taken to be: longitudinal modulus $E_L = 32$ GPa, transverse modulus $E_T = 4.6$ GPa, and longitudinal-transverse Poisson ratio $\nu_{LT} = 0.27$. The stiffness matrix for the $\pm\theta$ laminate is taken as the volume fraction weighted sum of the stiffness matrix for each layer, by the usual iso-strain assumptions of laminate plate theory. The strategy adopted is to use laminate plate theory to deduce the stress components $(\sigma_{cr}, \tau^{\infty})$ in the local tow axes, for the observed values of axial and shear stress (σ, τ) on the tube wall at failure. Relation (10)

Table 2. Critical elastic buckling stress and average buckle propagation load for compressive specimens failing by diamond shaped buckling

Helix angle	Critical elastic buckling stress (MPa)		Measured geometric variables for diamond shaped buckling			Buckle propagation load (kN)	
θ_o	Test	Model	m	n	ℓ (mm)	Test	Model
40°	43.6	87	3	3	42.2	3.5	3.5
55°	50.0	57.7	3	4	56	6	5.6

Table 3. The compressive and shear stresses in the local tow direction predicted from LPT, and the fibre waviness angle predicted from equation (10)

Test and fibre orientation θ_o	Macroscopic stress on tube wall (MPa)		Stresses along tow direction (MPa)		Waviness
	axial, σ	shear, τ	σ_{cr}	τ^{∞}	Predicted $\bar{\phi}$ (measured $\bar{\phi}$)
Compression					
23°	60	–	64.5	8.4	12.1° (10°)
Torsion					
23°	–	32	64.8	9.0	11.5° (10°)
40°	–	52	94.7	2.4	11.8° (10.5°)
55°	–	56	102	2.6	10.9° (9.5°)
Comp/torsion					
23°	35	25	88.2	2.2	12.9° (10°)
40°	25	48	112	8.3	7.0° (10.5°)
55°	28	52	114	17.5	2.2° (9.5°)

is then used to deduce the fibre waviness $\bar{\phi}$, using $k = 22$ MPa from independent measurements [4].

4.2.3. Comparison of theory with experiment for microbuckling mode. The tow stresses σ_{cr} and τ^{∞}, as determined by LPT, and the inferred values of $\bar{\phi}$ from (10) are listed in Table 3 for compression, torsion and combined compression–torsion tests. The actual fibre undulation at tow cross-overs was also measured using a scanning electron microscope (SEM), and compared with the predicted values in Table 3 and in Fig. 11. Most of the calculated values are in good agreement with the measured values. The exception is the $\theta_o = 55°$ braid tested under combined loading, which may not have failed purely by microbuckling: post-mortem examination revealed that the specimen underwent diamond shaped buckling in addition to microbuckling.

5. STRUCTURAL OPTIMISATION OF BRAIDED TUBES IN COMPRESSION

Following the method of Weaver and Ashby [14], we next explore the effect of tube geometry upon the dominant failure mode for braided tubes in compression: Euler buckling, diamond shaped buckling or microbuckling. Euler buckling is the overall lateral collapse of the structure. Diamond shaped buckling is an elastic buckling of the tube wall, and microbuckling is a local material instability.

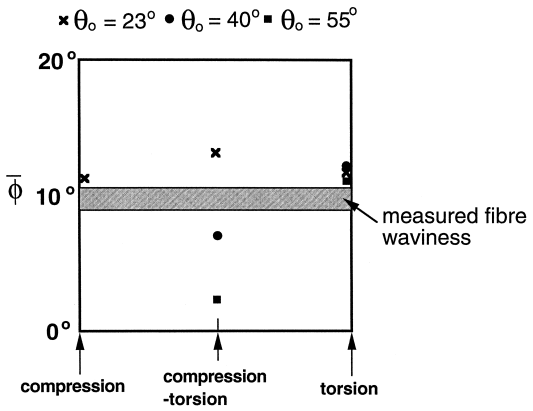

Fig. 11. Comparison of the calculated values of fibre waviness angle (discrete data points) with the experimental values (shaded band).

The geometry of the tube determines which failure mode dominates. For example, Euler buckling dominates for long slender tubes. It is instructive to map the various regimes of collapse mode and to calculate the *efficiency* of the tube, that is the load bearing capacity for minimum weight, as a function of the geometric variables. On writing the cross-sectional area A of the wall of a tube as:

$$A = 2\pi r t \tag{11}$$

and its second moment of area, I, as

$$I = \pi r^3 t \tag{12}$$

the shape factor Φ, defined as $\Phi \equiv r/t$, can be re-expressed as

$$\frac{\Phi}{4\pi} = \frac{I}{A^2} \tag{13}$$

Consider each collapse mode in turn. Euler buckling of a tubular column of height ℓ and cross-sectional area A, with ends free to rotate, occurs at the load

$$P = \frac{\pi^2 EI}{\ell^2} \tag{14a}$$

where E is Young's modulus for the material. In reality, the end condition for a tubular column compressed between parallel plates falls somewhere between pin-jointed and built-in. The pin-jointed end condition gives the lowest Euler buckling load, and is employed herein. The axial stress in the tube wall σ_1 at the onset of Euler buckling follows as

$$\sigma_1 = \left(\frac{\pi}{4} \cdot E\Phi \cdot \frac{P}{\ell^2}\right)^{1/2} \tag{14b}$$

Diamond shaped buckling occurs in thin walled tubes when the axial stress exceeds, approximately, the value [6, 7]

$$\sigma_2 = 0.6\alpha\frac{E}{\Phi} \tag{15}$$

This equation is identical in form to equation (2) with α being the knockdown factor to take into account the effect of imperfections in the tube, and the effect of anisotropy. Young [15] uses a factor of 0.5, whereas Weingarten *et al.* [7] have shown that the knockdown increases from 0.5 and 0.8 with increasing r/t. A value of 0.5 is used here.

The microbuckling strength σ_3 depends upon the shear strength of the matrix, k and the initial misalignment of the fibres $\bar{\phi}$,

$$\sigma_3 \approx \frac{k}{\tan\ \bar{\phi}} \tag{16}$$

directly from (9). The boundaries between fields of dominance of each collapse mechanism is found by equating the equations for σ_1, σ_2 and σ_3 in pairs, giving

(1–2 boundary)

$$\frac{PE^2}{\ell^2k^3} = \frac{1.44\alpha^2}{\pi}\cdot\left(\frac{E}{k\Phi}\right)^3 \tag{17a}$$

(1–3 boundary)

$$\frac{PE^2}{\ell^2k^3} = \frac{4}{\pi\ \tan^2(\bar{\phi})}\cdot\frac{E}{k\Phi} \tag{17b}$$

(2–3 boundary)

$$\frac{k\Phi}{E} = 0.6\alpha\ \tan\ \bar{\phi} \tag{17c}$$

The above variables have been grouped into dimensionless groups PE^2/ℓ^2k^3 and $k\Phi/E$, reducing the number of independent groups to two. This allows for a simple presentation of the failure-mechanism boundaries, and the associated fields of dominance as shown in Fig. 12, for the assumed values of $\alpha = 0.5$ and $\bar{\phi} = 10^\circ$.

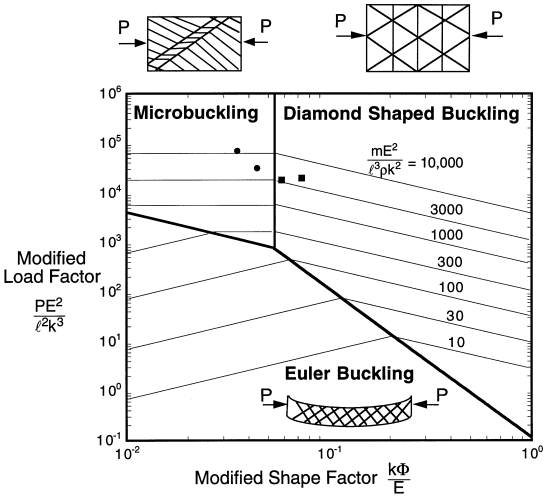

Fig. 12. Shape efficiency map for glass fibre/epoxy braided tubes. $\alpha = 0.5$, $\bar{\phi} = 10^\circ$. Experimental data are included. The solid circles denote specimens which failed by microbuckling and the solid squares denote specimens which failed by diamond shaped buckling.

In order to determine the structural efficiency of a tubular strut, we need a measure of the mass required to support a given load. The mass is given by

$$m = A\ell\rho \tag{18}$$

where A is the cross-sectional area of the tube wall and ρ is the density of the tube wall material. Within the Euler buckling regime, the minimum section area which will just support a load P is

$$A_1 = \frac{P}{\sigma_1} \tag{19}$$

Inserting this into equation (18) and replacing σ_1 by equation (14b) gives for Euler buckling

$$\frac{PE^2}{\ell^2k^3} = \frac{\pi}{4}\left(\frac{mE^2}{\rho\ell^3k^2}\right)^2\cdot\frac{k\Phi}{E} \tag{20a}$$

In the diamond shaped buckling field of dominance we find

$$\frac{PE^2}{\ell^2k^3} = 0.6\alpha\left(\frac{mE^2}{\rho\ell^3k^2}\right)\cdot\frac{E}{k\Phi} \tag{20b}$$

while for microbuckling we find

$$\frac{PE^2}{\ell^2k^3} = \left(\frac{mE^2}{\rho\ell^3k^2}\right)\frac{1}{\tan\ \bar{\phi}} \tag{20c}$$

As before, the variables have been clustered in dimensionless groups, with the mass described in $(mE^2/\rho\ell^3k^2)$. For a chosen value of this quantity, each equation becomes a relation between the modified load factor, PE^2/ℓ^2k^3, and the modified shape factor $k\Phi/E$ allowing contours of mass to be added to Fig. 12. Minimum weight design for a given modified load factor PE^2/ℓ^2k^3 is achieved by selecting the modified shape factor $k\Phi/E$ in order to minimise $mE^2/\rho\ell^3k^2$. Inspection of Fig. 12 shows that minimum weight designs occupy the whole field of microbuckling and the boundary between the failure modes of Euler buckling and diamond shaped buckling. The modified load and shape factors for the braids tested are included in Table 1 and the values have been included in Fig. 12. Only a limited test series was conducted due to the labour-intensive nature of the braid manufacture.

6. CONCLUDING REMARKS

The failure modes for braided tubes have been mapped as a function of braid angle and load path,

from the experimental results of the current study and from a related study on the tensile loading of braids by Harte and Fleck [4]. A failure surface is plotted in both stress space and strain space. The dominant mode has also been plotted in the form of a fracture map, with axes of loading direction and helix angle. The dominant failure modes are neck propagation and fibre failure in tension, fibre microbuckling and diamond shaped buckling in compression and microbuckling in torsion. It is found that braids of low helix angle ($\theta_o = 23^\circ$) fail by fibre failure in tension and by fibre microbuckling in compression. When the helix angle is increased to 55°, the elastic modulus, tensile strength and compressive strength drop whereas the ductility and energy absorption increase. Failure is by neck propagation in tension and by diamond shaped buckling in compression. Most of the failure modes are controlled by matrix properties, with fibre stiffness and strength playing a minor role. The exception is the fibre failure mode in tension.

Diamond shaped bucking and microbuckling were modelled using simple mechanics models. In order for diamond shaped buckling to occur, a peak initiation stress must be attained before buckling can progress at a lower load. Using existing models for microbuckling in composites, an estimate was made for the waviness angle at the cross-over points of the tows. Predictions of the waviness angle of the braid were satisfactory, and it is tentatively concluded that the microbuckling analysis which has been derived for traditional laminate composites can also be successfully applied to braided composites.

Acknowledgements—The authors wish to thank the Natural Sciences and Engineering Research Council of Canada, the Newton Trust, and DARPA/ONR through MURI grant number N00014-1-96-1028 for their financial support; they are grateful to Cambridge Consultants Ltd for the provision of test materials and to Professor M. F. Ashby for helpful discussions.

REFERENCES

1. Cronkhite, J. D., Design of helicopter composite structures for crashworthiness. Presented at the *5th International SAMPE Technical Symposium—Design and use of Kevlar Aramid Fiber in Composite Structures*, Reno, Nevada, 1984.
2. Hamada, H., Ramakrishna, S., Nakamura, M., Maekawa, Z. and Hull, D., *Composites Interfaces*, 1994, **2**, 127.
3. Chou, T.-W., *Microstructural Design of Fiber Composites*. Cambridge University Press, Cambridge, 1992.
4. Harte, A.-M. and Fleck, N. A., *Eur. J. Mech. A/Solids*, in press.
5. Fleck, N. A., *Advances in Applied Mechanics*, Vol. 33, Academic Press, New York, 1997, pp. 43–119.
6. Timoshenko, S. P. and Gere, J. M., *Theory of Elastic Stability*. McGraw-Hill, New York, 1961.
7. Weingarten, V. I., Seide, P. and Peterson, J. P., Buckling of thin-walled circular cylinders. *NASA Space Vehicle Design Criteria*. National Aeronautics and Space Administration, Rept No. NASA SP-8007, 1968.
8. Pugsley, A. and Macaulay, M., *Quart. J. Mech. Applied Math*, 1960, **13**, 1.
9. Johnson, W., Soden, P. D. and Al-Hassini, S. T. S., *J. Strain Anal.*, 1977, **12**(4), 317.
10. Al-Hassani, S. T. S., Johnson, W. and Lowe, W. T., *J. Mech. Eng. Sci.*, 1972, **14**(6), 370.
11. Harte, A.-M., The mechanics of braided composites. Ph.D. Thesis, Cambridge University, 1997.
12. Argon, A. S., *Treatise of Materials Science and Technology*, Vol. 1. Academic Press, New York, 1972.
13. Fleck, N. A. and Budiansky, B., in *Proc. IUTAM Symp. on Inelastic Deformation of Composite Materials, Troy, New York*. Springer-Verlag, Berlin, 1991.
14. Weaver, P. M. and Ashby, M. F., *An overview of material limits for shape efficiency*. Cambridge University Engineering Departmental Report, 1997.
15. Young, W. C., *Roark's Formulas for Stress and Strain*. McGraw-Hill, New York, 1989.